Blast waves in a paraxial fluid of light (a)

Murad Abuzarli, Tom Bienaimé, Elisabeth Giacobino, Alberto Bramati, Quentin Glorieux

LETTER

Blast waves in a paraxial fluid of light[(a)]

To cite this article: M. Abuzarli *et al* 2021 *EPL* **134** 24001

A Letters Journal Exploring the Frontiers of Physics

April 2021

EPL, **134** (2021) 24001
doi: 10.1209/0295-5075/134/24001

www.epljournal.org

Focus Article

Blast waves in a paraxial fluid of light[(a)]

M. Abuzarli, T. Bienaimé, E. Giacobino, A. Bramati and Q. Glorieux[(b)]

Laboratoire Kastler Brossel, Sorbonne Université, CNRS, ENS-Université PSL, Collège de France - Paris, France

received 22 January 2021; accepted in final form 1 April 2021
published online 19 May 2021

Abstract – We study experimentally blast wave dynamics on a weakly interacting fluid of light. The fluid density and velocity are measured in 1D and 2D geometries. Using a state equation arising from the analogy between optical propagation in the paraxial approximation and the hydrodynamic Euler's equation, we access the fluid hydrostatic and dynamic pressure. In the 2D configuration, we observe a negative differential hydrostatic pressure after the fast expansion of a localized over-density, which is a typical signature of a blast wave for compressible gases. Our experimental results are compared to the Friedlander waveform hydrodynamical model (Friedlander F. G., *Proc. R. Soc. A: Math. Phys. Sci.*, **186** (1946) 322). Velocity measurements are presented in 1D and 2D configurations and compared to the local speed of sound, to identify the supersonic region of the fluid. Our findings show an unprecedented control over hydrodynamic quantities in a paraxial fluid of light.

Introduction. – In classical hydrodynamics, a blast wave is characterized by an increased pressure and flow resulting from the rapid release of energy from a concentrated source [1]. The particular characteristic of a blast wave is that it is followed by a wind of negative pressure, which induces an attractive force back towards the origin of the shock. Typical blast waves occur after the detonation of trinitrotoluene [2,3], nuclear fission [4], break of a pressurized container [5] or heating caused by a focused pulsed laser [6]. The sudden release of energy causes a rapid expansion, which in a three-dimensional space is analogous to a spherical piston [7] and produces a compression wave in the ambient gas. For a fast enough piston, the compression wave develops into a shock wave which is characterized by the rapid increase of all the physical properties of the gas, namely, the hydrostatic pressure, density and particle velocity [8]. In 1946, Friedlander predicted that immediately after the shock front the physical properties at a given position in space decay exponentially [9]. In this model, for 3-dimensional and 2-dimensional spaces the hydrostatic pressure and the density are expected to fall below the values of the ambient atmosphere leading to a blast wind [1].

Shock waves have been studied in several contexts in physics, including acoustics, plasma physics, ultra-cold atomic gases [10–12] and non-linear optics [5,13–15]. In optics, the hydrodynamics interpretation relies on the Madelung transforms which identify the light intensity to the fluid density and the phase gradient to the fluid velocity [16]. Recently several works have studied analytically shock wave formation in one and two dimensions [17,18]. Optical systems allow for repeatable experiments and precise control of the experimental parameters. For example dispersive superfluid-like shock waves have been observed [13], as well as generation of solitons [14], shocks in non-local media [19], shocks in disordered media [15], analogue dam break [5] and Riemann waves [20]. However, an experimental study of blast waves has not been done in atomic gases nor in non-linear optics systems. In this work, we demonstrate the generation of a blast wave in a fluid of light. Interestingly, the prediction of a blast wind with negative pressure and density holds in a two-dimensional space but not in 1 dimension [21]. Optical analogue systems allow for an experimental validation of this prediction.

In this letter, we study the formation of blast waves in a paraxial fluid of light. We measure the time evolution of analogue physical properties such as the hydrostatic pressure, the density, the particle velocity and the dynamic pressure at a fixed point for 1- and 2-dimensional systems. We report the observation of a negative hydrostatic

[(a)] Contribution to the Focus Issue *Turbulent Regimes in Bose-Einstein Condensates* edited by Alessandra Lanotte, Iacopo Carusotto and Alberto Bramati.

[(b)] E-mail: quentin.glorieux@lkb.upmc.fr (corresponding author)

differential pressure after a shock wave in a 2-dimensional system and we show that the Friedlander waveform describes quantitatively our experimental results for all physical parameters. This paper is organized as follows. We first introduce the analogy between the propagation equation of a laser beam through a non-linear medium (a warm atomic vapor) and the hydrodynamics equation and derive the relevant analogue physical properties. In the second section of this work, we describe our experimental setup and present our results on the density and hydrostatic pressure measurements. We highlight the striking differences between 1- and 2-dimensional systems. Finally, we study the time evolution of the velocity and dynamic pressure.

Theoretical model. – We describe the propagation of a linearly polarized monochromatic beam in a local Kerr medium. We separate the electric field's fast oscillating carrier from the slowly varying (with respect to the laser wavelength) envelope: $E = \mathcal{E}(\mathbf{r}, z)\mathrm{e}^{i(kz-k_0ct)}+$ complex conjugate, where k and k_0 are the laser wave vectors respectively in the medium and in vacuum. Under the paraxial approximation, the propagation equation for the envelope $\mathcal{E}$ is the Non-Linear Schrödinger Equation (NLSE) [16]:

$$i\frac{\partial\mathcal{E}}{\partial z} = \left(-\frac{1}{2k}\nabla_\perp^2 + g|\mathcal{E}|^2 - \frac{i\alpha}{2}\right)\mathcal{E}, \tag{1}$$

where α is the extinction coefficient accounting for losses due to absorption (see the Supplementary Material `Supplementarymaterial.pdf` (SM) for more details), and the g parameter is linked to the intensity-dependent refractive index variation Δn via: $g|\mathcal{E}|^2 = -k_0\Delta n$.

The NLSE is analogous to a 2D Gross-Pitaevskii equation describing the dynamics of a quantum fluid in the mean-field approximation. This analogy is possible by mapping the envelope $\mathcal{E}$ to the quantum fluid many-body wave function and the axial coordinate z to an effective evolution time. The non-linear refractive index variation plays then the role of a repulsive photon-photon interaction, since all measurements in this work are done in the self-defocusing regime, *i.e.*, $\Delta n < 0$ and therefore $g > 0$. Diffraction acts as kinetic energy with the effective mass emerging from the paraxial approximation and given by the laser wave vector $k = 8\cdot10^6\,\mathrm{m}^{-1}$. Using the Madelung transformation: $\mathcal{E} = \sqrt{\rho}\mathrm{e}^{i\phi}$, $\mathbf{v} = \frac{c}{k}\nabla_\perp\phi$ one can derive from the NLSE hydrodynamic equations [13,17], linking the fluid's density ρ with its velocity $\mathbf{v}$:

$$\frac{\partial\rho}{\partial z} + \nabla_\perp.\left(\rho\frac{\mathbf{v}}{c}\right) = -\alpha\rho, \tag{2}$$

$$\frac{\partial\mathbf{v}}{\partial z} + \frac{1}{2c}\nabla_\perp\mathbf{v}^2 = -\nabla_\perp\left(\frac{cg\rho}{k} - \frac{c}{2k^2\sqrt{\rho}}\nabla_\perp^2\sqrt{\rho}\right). \tag{3}$$

Equation (2) is the continuity equation with a loss term accounting for photon absorption. Equation (3) is similar to the Euler equation without viscosity, in which the driving force stems from interaction and the so-called quantum pressure term due to diffraction. Establishing the formal analogy requires, however, defining an analogue pressure P to be able to re-express the right-hand side of eq. (3) as $-1/\rho\cdot\nabla_\perp P$. This is possible for the first term stemming from interactions. Using the identity $-\nabla_\perp\rho = -1/(2\rho)\nabla_\perp\rho^2$ one can define the so-called bulk hydrostatic pressure P as

$$P = \frac{c^2}{2}\frac{\rho^2 g}{k} = \frac{1}{2}\rho c_s^2, \tag{4}$$

where the last equality comes from $c_s^2 = c^2\cdot g\rho/k$. Equation (4) is the state equation linking the fluid hydrostatic pressure P to its density if one neglects the quantum pressure term (see the SM for more details). It is the consequence of the mean-field formulation of the interaction. It also implies that the fluid of light is compressible with the compressibility equal to $k/(c^2\rho^2 g)$. One then gets the analogue Euler equation:

$$\frac{\partial\mathbf{v}}{\partial(z/c)} + \frac{1}{2}\nabla_\perp\mathbf{v}^2 = -\frac{1}{\rho}\nabla_\perp P, \tag{5}$$

with a pressure P of dimension $[density]\times[speed]^2$. As already mentioned, the fluid dynamics can be studied by accessing its state at different z positions, however this is not recommended practically since imaging inside a nonlinear medium is a highly challenging task. Alternatively, one can instead re-scale the effective time by incorporating fluid interaction [18,22]. Fluid interaction can then be varied experimentally and the fluid dynamics can be studied while imaging only the state at the medium output plane. Re-scaling the time is based on defining the following quantities:

$$z_{NL} = \frac{1}{g\rho(0,L)}, \quad \text{non-linear axial length,} \tag{6}$$

$$\xi = \sqrt{\frac{z_{NL}}{k}}, \quad \text{transverse healing length,} \tag{7}$$

$$c_s = \frac{c}{k\xi}, \quad \text{speed of sound,} \tag{8}$$

$$\psi = \frac{\mathcal{E}}{\sqrt{\rho(0,L)}}, \tag{9}$$

and substituting the time and space variables as $\tau = z/z_{NL}$, $\tilde{\mathbf{r}} = \mathbf{r}/\xi$, $\tilde{\nabla}_\perp = \xi\nabla_\perp$. L is the non-linear medium length. The propagation equation then reads

$$i\frac{\partial\psi}{\partial\tau} = \left(-\frac{1}{2}\tilde{\nabla}_\perp^2 + |\psi|^2\right)\psi. \tag{10}$$

One can note that the dynamics of ψ is not dissipative anymore, due to the normalization with respect to the exponentially decaying density $\rho(0,L) = \rho(0,0)\exp(-\alpha L)$, measured at the medium exit plane and provided a redefinition of the interaction parameter by its average over the propagation within the cell. This formulation is necessary to describe accurately the experimental results of this work probing the temporal dynamics of a

fluid of light by varying the strength of the optical non-linearity and not the imaged z-plane. The effective time $\tau = |\Delta n(\mathbf{r}_\perp = 0, L)|k_0 L$ equals the maximal accumulated non-linear phase. Rewriting the Madelung transformation with the new variables, we obtain

$$\psi = \sqrt{\tilde{\rho}}\mathrm{e}^{i\phi} = \sqrt{\frac{\rho}{\rho(0,L)}}\mathrm{e}^{i\phi}, \qquad \tilde{\mathbf{v}} = \frac{\mathbf{v}}{c_s} = \tilde{\nabla}_\perp \phi. \quad (11)$$

One gets dimensionless Euler and the continuity equations:

$$\frac{\partial \tilde{\rho}}{\partial \tau} + \tilde{\nabla}_\perp \cdot (\tilde{\rho}\tilde{\mathbf{v}}) = 0, \quad (12)$$

$$\frac{\partial \tilde{\mathbf{v}}}{\partial \tau} + \frac{1}{2}\tilde{\nabla}_\perp \tilde{\mathbf{v}}^2 = -\tilde{\nabla}_\perp \left(\tilde{\rho} - \frac{1}{2\sqrt{\tilde{\rho}}}\tilde{\nabla}_\perp^2 \sqrt{\tilde{\rho}} \right), \quad (13)$$

where the link between eq. (13) and the Euler equation is made by neglecting the quantum pressure and defining the dimensionless hydrostatic pressure as

$$\tilde{P} = \frac{1}{2}\tilde{\rho}^2. \quad (14)$$

Finally, the dynamic pressure is defined as a vector quantity by

$$\tilde{P}_d = \frac{1}{2}\tilde{\rho}\tilde{\mathbf{v}}|\tilde{\mathbf{v}}|. \quad (15)$$

The dynamic pressure is the fluid kinetic energy flux and accounts for the amount of pressure due to fluid motion. The impact force on an obstacle hit by a shockwave is proportional to its dynamic pressure. Expressed in dimensionless units, the dynamic pressure gives the strength of the convection term normalized by the pressure due to the interactions in eq. (13). It can be computed directly from the density and velocity measurements.

Shock waves and blast wind. – In this work, we study the dynamics of a fluid of light disturbed by a localized Gaussian over-density $\delta\rho(\mathbf{r}, 0) = \rho_1 \exp(-2\mathbf{r}^2/\omega_1^2)$. ρ_1 is of the same magnitude as the background fluid density ρ_0 and ω_1 quantifies the perturbation width. We can write $\rho(\mathbf{r}, L) = \rho_0(\mathbf{r}) + \delta\rho(\mathbf{r}, L)$. Indeed $\tilde{\rho}_0$ depends on r having a Gaussian shape, much larger than ω_1. Normalizing the total density by its maximal undisturbed value one gets $\tilde{\rho}(\mathbf{r}, \tau) = \rho(\mathbf{r}, L)/\rho_0(0, L)$. Extending this definition to ρ_0 and ρ_1, we obtain $\tilde{\rho}_0$ bound between 0 and 1, and $\tilde{\rho}_1$ expressing the perturbation strength with respect to the fluid background density. We define the over-density and the over-pressure from the pressure difference between the case with and without perturbation:

$$\delta\tilde{\rho}(\mathbf{r}, \tau) = \tilde{\rho}(\mathbf{r}, \tau) - \tilde{\rho}_0(\mathbf{r}, \tau), \quad (16)$$

$$\delta\tilde{P}(\mathbf{r}, \tau) = \tilde{P}(\mathbf{r}, \tau) - \tilde{P}_0(\mathbf{r}, \tau), \quad (17)$$

where the over-pressure is calculated using eq. (14). To evaluate the differential pressure $\Delta\tilde{P}(\tau)$, showing the instantaneous difference in pressure between the perturbation center and the external undisturbed area, we define

$$\Delta\tilde{P}(\tau) = \tilde{P}(0, \tau) - P_0(r_{ext}, \tau). \quad (18)$$

The differential pressure $\Delta\tilde{P}(\tau)$ is the most important quantity we study in this work and we expect major differences in the non-linear perturbation dynamics between the 1D and the 2D geometries. Finally, the fluid velocity can be measured experimentally. It requires a measurement of the beam wavefront which is realized using off-axis interferometry. Calculating numerically the gradient of the phase, we obtain the background fluid velocity $\mathbf{v}_0$ and the perturbation velocity $\mathbf{v}_1$ by analyzing the images without and with the perturbation, respectively.

Several studies have been performed in both $\rho_1 \ll \rho_0$ and $\rho_1 \gg \rho_0$ regimes, observing the Bogoliubov dispersion of the linearized waves created by the perturbation [23–25], and the shock waves [13,18], respectively. In this work we investigate the case $\rho_1 \sim \rho_0$ by analyzing the fluid density, velocity and pressure both in the 1D and 2D geometries. The NLSE is known to give rise to sound-like dispersion to the low amplitude waves, governed by the Bogoliubov theory. Here, a perturbation of the same order (or larger) than the background results in the sound velocity variation following the local density inside the perturbation. This is the prerequisite for observing shock waves, a special type of waves changing their shape during propagation towards a steepening profile. In hydrodynamics, shock waves are usually reported as a time evolution measurement of a physical quantity (pressure, density...) at a fixed point in space. After the passage of a the shock wave front, a blast wind (a negative differential pressure) should be observed in 2- and 3-dimensional space. A direct physical consequence of this wind in classical hydrodynamics is observed for example after an explosion inside an edifice: the presence of glass pieces within the building is the signature of the blast wind. In the next section we report the time evolution as well as the time snapshots (spatial map of a physical quantity at fixed time) typically not accessible in classical hydrodynamics experiments.

Experimental setup. – In our experiment, we investigate the propagation of a near-resonance laser beam through a 75 mm long warm ^{85}Rb vapor cell, which induces effective photon-photon interactions [26]. Two configurations are studied: the 2D geometry with a radially symmetric dynamics and the 1D geometry with a background much larger along x than along y which allows for a 1D description of non-linear wave dynamics [18]. The experimental setup is schematically visualized in fig. 1(a). A tapered amplified diode laser beam is mode cleaned with a polarization maintaining single-mode fiber and then split into a background, a reference and a perturbation beams (see the SM for details). The background beam is enlarged with a telescope up to a waist of 2.5 ± 0.5 mm along x and 0.8 ± 0.1 mm along y in the 1D geometry, and 1.8 ± 0.3 mm along the radial coordinate in the 2D configuration. The reference beam (for interferometric phase measurement) is matched to the same dimensions. The perturbation beam is focused to get the waist of 0.12 ± 0.03 mm in the middle of the cell (the corresponding Rayleigh range is 55 mm).

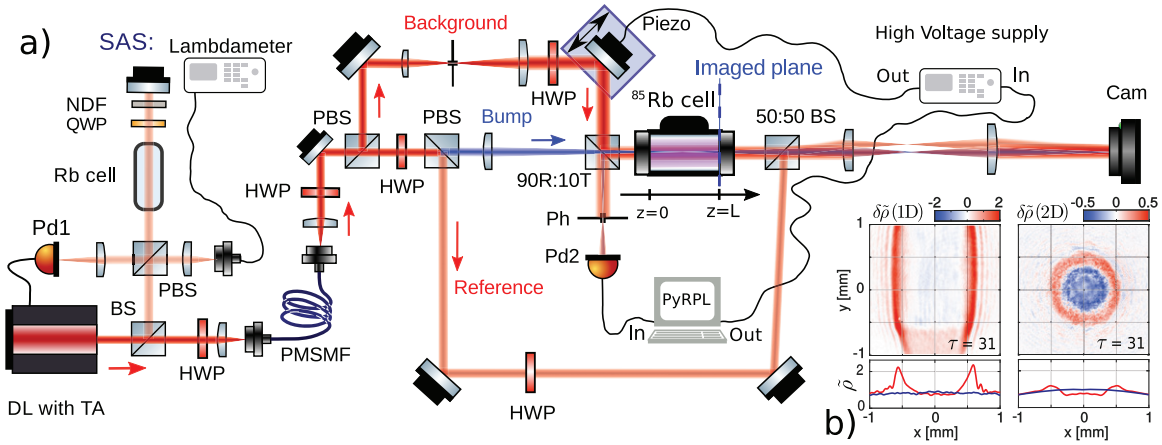

Fig. 1: (a) Experimental setup: laser frequency performed with Saturable Absorption Spectroscopy (SAS) and a MogWave Lambdameter. After mode cleaning with a Polarization Maintaining Single-Mode Fiber (PMSMF), the laser beam was split into the background, bump and the reference. The background-bump interference signal was measured by cropping the overlap area (200 μm diameter pinhole (Ph)) on a photodiode (Pd2) on the beam splitter arm complementary to the Rb vapor cell. This signal was transformed via the PyRPL lockbox software into an error signal driving the piezoelectric mirror mount (piezo) to lock the (Pd2) signal on a minimum. This relative phase control enables permanent constructive interference on the vapor cell arm. (b) Over-density images obtained by image subtraction (see eq. (16)) in the 1D and 2D cases, revealing appearance of negative over-density in the 2D case. The centered unperturbed (blue) and perturbed (red) density profiles are shown below.

The background and perturbation are recombined with a 90R:10T beam splitter such that 90% of the background beam power is reflected towards the cell. The second arm of the BS is sent through a 200 μm diameter pinhole into a photodiode to stabilize the interferometer. The control is realized by locking on local minimum acting on a piezoelectric mirror mount with a RedPitaya FPGA run by the PyRPL software [27]. Cell temperature is $149 \pm 2\,^{\circ}$C leading to an atomic density of $8.3 \pm 0.8 \times 10^{13}\,\mathrm{cm}^{-3}$. The cell output is imaged with a $\times 4.2$ magnifying 4-f setup onto a camera. Sets of 4 images (background only, background with reference, background with perturbation and finally background with both perturbation and reference) at different input powers $\mathcal{P}$ ranging from 50 to 600 mW and different laser detunings Δ from the ^{85}Rb D2 line $F = 3 \rightarrow F'$ transition are taken (see the SM for details). The reference beam is superimposed with other beams with an angle of 30 milli-radians, giving rise to interferograms with vertical fringes of average periodicity of $25 \pm 1\,\mu$m. By changing the laser intensity and detuning, we can modify the effective time τ. The associated time τ is calculated from the nonlinear index Δn via the off-axis interferometric measurement for each experimental configuration $(\mathcal{P}, \Delta)$ (see the SM for details).

Density. – The density is an important physical parameter needed to compute the static and hydrodynamic pressure. It is directly given by the intensity measurement. In fig. 1(b) we present the experimental images of the over-density $\delta\tilde{\rho}$ at time $\tau = 31$, using image subtraction as described in eq. (16), in the 1D and 2D geometries, respectively. From this images, as well as the corresponding centered profiles given below, one can notice the key difference in the evolution of the bump in both geometries: the appearance of a negative over-density after the bump's expansion (corresponding to times above $\tau > 20$) in the 2D geometry. Interestingly, this effect seems absent in the 1D case, which, on the contrary, shows clear steepening of the perturbation front and the development of dispersive shock waves in form of an oscillating pattern developing beyond the shock front with effective time τ, the effect less pronounced in the 2D case. These features have direct consequences on the evolution of the over-pressure and the differential pressure. The negative differential density has a direct consequence on the sign change in the differential pressure calculated using eq. (18).

Static pressure. – To isolate the effect of the perturbation on the static pressure, we compute the over-pressure from images of the background with and without the bump taken at same effective times $\tau(\mathcal{P}, \Delta)$, using eqs. (17) and (14). The over-pressure as a function of time τ is shown in figs. 2(b) and (d) and profiles averaged along y in the 1D case and radially in the 2D case are presented in figs. 2(a) and (c) for various times.

The trajectory of a density pulse spreading with no dispersion at the speed of sound can be expressed as follows: $r = c_s(\tau) \times (L/c)$. The coefficient can be calculated using the time dependence of the sound velocity: $c_s = c\sqrt{\tau/(kL)}$ obtained from eqs. (6) and (8). It directly leads to $\tau = kr^2/L$ and knowing that $L = 75\,\mathrm{mm}$ and $k = 8 \times 10^3\,\mathrm{mm}^{-1}$, one gets: $\tau = 107 \times r^2$. The coefficient does not depend on the dimensionality of the system.

In the pressure maps (figs. 2(b) and (d)), we have added a black dashed line following this trend: $\tau = 107 \times x^2$ (1D) and $\tau = 107 \times r^2$ (2D). As expected, this trajectory follows closely the shock front in the 1D geometry. The differential pressure is defined as the pressure difference between

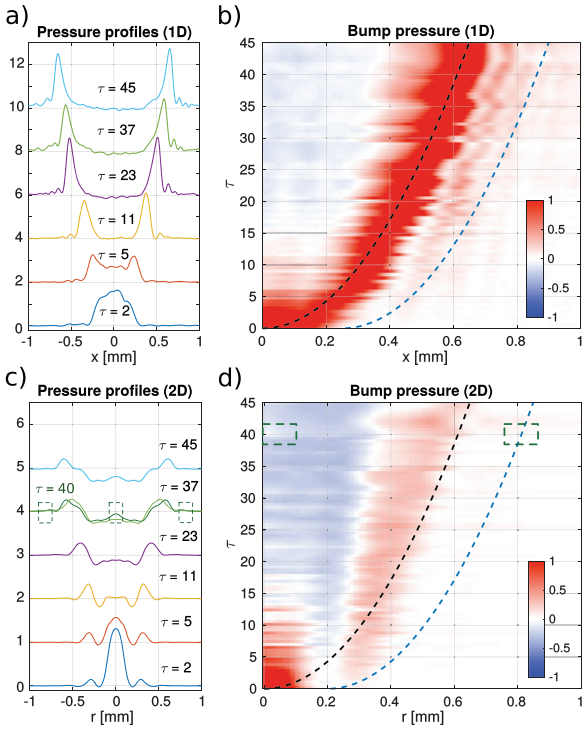

Fig. 2: Pressure analysis: ((a), (c)) over-pressure profiles evaluated at different effective times τ. Each following profile shifted vertically by 2 for better visibility. Panels (b), (d) show the 1D and 2D spatio-temporal diagrams of the over-pressure evolution, respectively. The dotted black lines show an expansion trajectory at the speed of sound according to $\tau = kr^2/L$, ($k/L = 107\,\mathrm{mm}^{-2}$) in both geometries. The blue dotted lines show the same trajectories shifted horizontally by 250 μm in the 1D (200 μm in 2D) case, used as external undisturbed area used for the measurement of the differential pressure. Dashed green rectangles around $\tau = 40$ show the presence of a second shock due to an increasing differential pressure.

inside and outside of the shock as expressed in eq. (18). The undisturbed pressure as a function of time is evaluated along the same trend line $\tau = 107 \times (r_{ext} - r_0)^2$, translated $r_0 = 250\,\mu$m in 1D and $r_0 = 200\,\mu$m in 2D, which corresponds to ~ 1.5 times the perturbation beam waist (blue dashed line). In 2D, the shock front expansion is slower than the calculated trajectory, as described in [18], and the blue dashed line can therefore still be used to define the undisturbed pressure.

The temporal evolution of the differential static pressure (at $x = 0$) is presented in fig. 3. 1D (red circles) and 2D (gray triangles) geometries are compared from $\tau = 0$ to $\tau = 45$. An important difference can be seen between the two geometries: in the 2D situation the differential pressure becomes negative at $\tau = 20$ as it goes to zero in the 1D case. The observation of the negative pressure is the typical signature of a blast wind. This measurement reveals the dramatic impact of the geometry on blast wind in a fluid of light and exemplifies the analogy with classical hydrodynamics. To quantify this analogy, we use the Friedlander waveform model which is known to describe

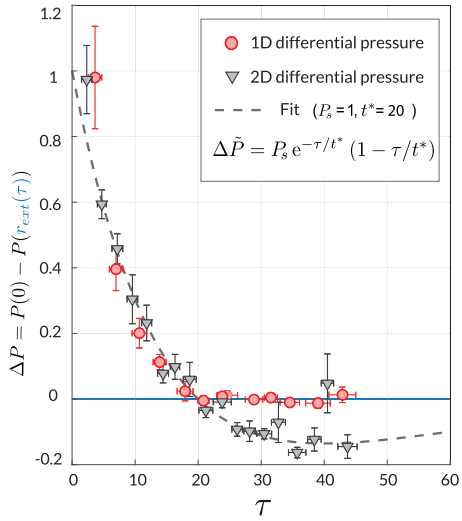

Fig. 3: Differential pressure calculated from eq. (18) for the 1D (circular dots) and the 2D cases (square dots). The uncertainty bars correspond to the statistical analysis of multiple images. The pressure is normalized as described in the main text. The blue line is the ambient pressure outside of the shock. The black dashed line is the Friedlander model for a blast wave described in eq. (19) with $P_s = 1$ and $t^* = 20$ obtained from fit to experimental data.

the dynamics of physical quantities in a free-field (*i.e.*, in an open 3-dimensional space) blast wave [1]. In this model the differential pressure follows an exponential decay of the form

$$\Delta\tilde{P} = P_s e^{-\tau/t^*}(1 - \tau/t^*), \tag{19}$$

where P_s and t^* are two parameters which correspond respectively to the peak differential pressure immediately behind the shock and to the time when the differential pressure becomes negative. The period when the hydrostatic pressure is above the ambient value is known as the positive phase, and the period when the properties are below the ambient value is the negative phase. We use $P_s = 1$ (since the differential pressure is normalized) and $t^* = 20$ (the parameters best fitting the experimental data) and plot the corresponding model with a black dashed line in fig. 3. An intriguing feature can also be seen in the 2D time evolution at $\tau = 40$. Close to the minimum of the negative phase, a second peak of differential pressure is observed (the single point at $\tau = 40$ fig. 3 is the average of several realizations with errors bars indicating the standard deviation of the measurement) in our optical analogue which is reminiscent of the second shock observed in classical explosion. In classical blast wave dynamics, this second shock is believed to be a consequence of the expansion and subsequent implosion of the detonation products and source materials. Our results suggest that this second shock might be of more general nature than currently thought.

Velocity. – For blast waves, there are no simple thermodynamic relationships between the physical properties

of the fluid at a fixed point [28]. This means that the temporal evolution of the static pressure measured at a fixed point is not sufficient to calculate the temporal evolution of the velocity or the dynamic pressure from that single measurement. To fully describe the physical properties of a fluid in a blast wave it is necessary to independently measure at least three of the physical properties, such as the static pressure, the density and the fluid velocity or the dynamic pressure. In the last section of this work, we report the measurement of the last two physical properties, which are vector quantities.

The fluid velocity is calculated from its phase (see eq. (11)) which is measured using off-axis interferometric imaging. The off-axis configuration consists in the tilted recombination of the signal beam with the reference beam on the camera plane. This results in the set of linear fringes evolving along the relative tilt direction and locally deformed (stretched or compressed) according to the beams relative curvature. Using a collimated Gaussian beam as the reference, the measured curvature is the one of the signal beam. The acquired interferogram carries the information on the beam phase via its amplitude modulated term. This term shows spatial periodicity and in the Fourier space it translates to two peaks shifted by a distance proportional to the off-axis tilt angle, symmetric with respect to the origin. By numerically calculating the spatial spectrum and filtering one of these peaks, the inverse Fourier transform gives the beam complex envelope with a spatial resolution bound by the fringe wavelength. The measured phase is unwrapped and the contribution due to the relative tilt is removed by subtracting the phase ramp. The resulting phase is averaged and numerically differentiated to get the velocity map.

Using this procedure, the off-axis interferograms of the background fluid and of the background fluid with the perturbation are analyzed to give access to $v_0(r,\tau)$ and $v(r,\tau)$, respectively. The difference of these quantities gives the perturbation velocity $v_1(r,\tau)$. The non-zero velocity v_0 of the background fluid arises from its finite size causing its expansion due to a non-zero pressure gradient. The knowledge of v_0 is essential to calculate the effective interaction g and therefore the time τ and the sound velocity. Indeed, $\phi_0 = \tau\tilde{\rho}_0$ can be accessed by integrating v_0 over the transverse coordinate and using the fact that $\phi(\tilde{r}\to\infty,\tau)\to 0$. Knowing τ, the sound velocity is $c_s(\mathbf{r}_\perp,\tau) = c\sqrt{\tau\tilde{\rho}_0(\mathbf{r}_\perp,\tau)/(k_0 L)}$.

The velocity maps normalized by the local sound velocity (in Mach units) are presented in figs. 4(a) and (b) for the 1D and 2D configurations, respectively. Since velocity is a vector quantity, negative values correspond to a propagation along $-x$ direction. Figures 4(c) and (d) show the corresponding profiles obtained for three specific times $\tau = 2;\ 23$ and 45. The maximal speed of sound at these times is 0.18, 0.62 and 0.86 percent of the speed of light in vacuum. Positive outward velocity, as well as zero velocity at the center is observed at all times both in the 1D and 2D cases. Whereas it is intuitively expected in the 1D geometry with the differential pressure never dropping to negative values, it also holds in the 2D case in which a negative phase for the differential pressure exists. A possible explanation lies in the fact that when the negative phase is reached for the differential pressure, the perturbation has already expanded enough such that the net resulting force is smaller due to a larger distance. It is also worth noting that the velocity is at least 2 times larger in the 1D geometry than in 2D, as seen by comparison of the y-axis scales in figs. 4(c) and (d). Additionally, clear steepening of the velocity profiles is observed in the 1D case reaching a Mach number of 1 at the steepest position.

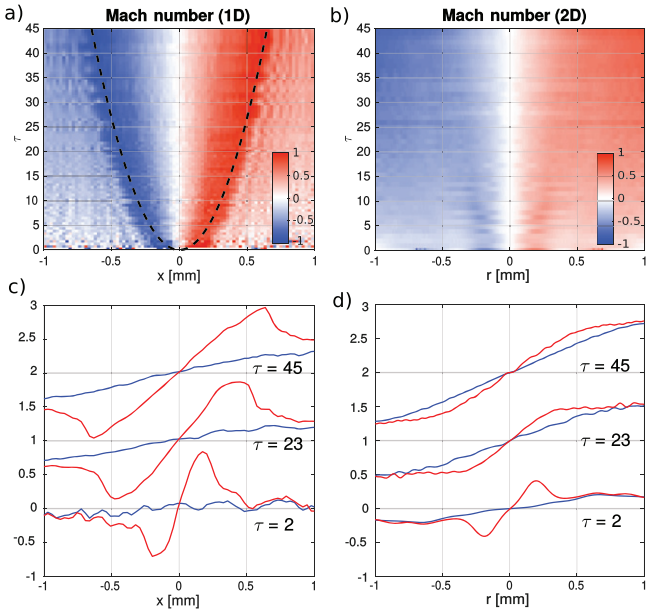

Fig. 4: Fluid velocities from the off-axis interferometry. (a), (b): space-time evolution of the Mach number with respect to the background's local speed of sound, in the 1D and 2D geometry, respectively. The dotted black line in (a) shows the calculated trajectory of expansion at the speed of sound (see main text). Panels (c) and (d) show the background's $\tilde{v}_0$ (blue) and total $\tilde{v}$ (red) Mach number profiles, at different times, for the 1D (x-coordinate) and 2D geometry (radial coordinate), respectively. Each following profile shifted vertically (spacing of 1) for visibility.

Dynamic pressure. – Alternatively, we can measure the dynamic pressure to compute a third thermodynamic quantity: the total pressure. The dynamic pressure is also a vector quantity and can be obtained from a phase measurement similar to fluid velocity using eq. (15). The dynamic pressure maps are presented in figs. 5(a) and (b). Once again figs. 5(c) and (d) show dynamic pressure profiles for three selected times. In 1D, the dynamic pressure forms a steep overpressure characteristic of the shock front which increases as a function of time. In the 2D geometry, on the contrary, the dynamic pressure reaches a plateau at the shock front without forming a steep overpressure peak. This behavior is in agreement with the velocity distributions presented previously.

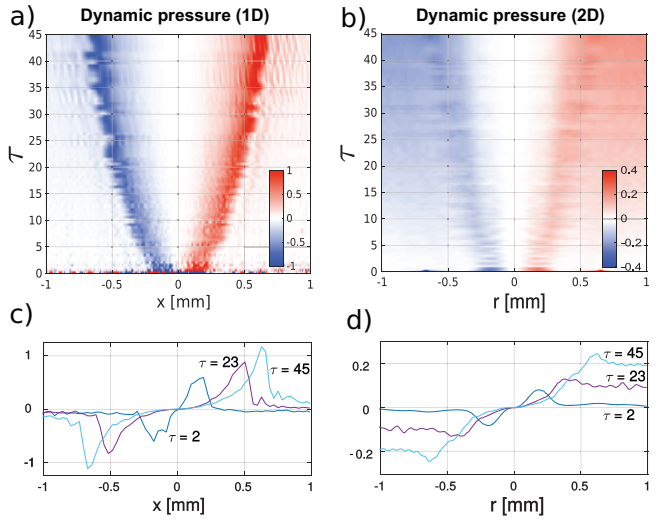

Fig. 5: Dynamic pressure analysis. Panels (a) and (b) show the spatio-temporal evolution maps of the dynamic pressure profiles, for the 1D (the x-component) and 2D geometry (the radial component), respectively. Below, panels (c) and (d) show various superimposed dynamic pressure profiles at different times, in 1D and 2D geometry, respectively.

Conclusion. – Relying on detailed measurements of all thermodynamic quantities in a fluid of light blast wave, we have demonstrated for the first time the occurence of a blast wave in a fluid of light. We compare 1D and 2D geometry and report the observation of a negative phase during the blast only for the 2-dimensional case. The differential pressure in the 2D geometry is compared to the classical hydrodynamics of Friedlander blast-wave and we see a very good agreement with this model. Velocity maps and dynamic pressure are finally presented to complete the study. Our work opens the way to precise engineering of a fluid of light density and velocity distribution which will prove to be a valuable tool to design new experiments studying superfluid turbulence [29] or analogue gravity where an excitation of a fluid of light changes from a subsonic to a supersonic region.

* * *

The authors thank F. Claude and S. Deléglise for useful discussions for setting up PyRPL. This work is supported by the European Union Horizon 2020 Research and Innovation Program under Grant Agreement No. 820392 (PhoQuS).

REFERENCES

[1] Dewey J. M., *Measurement of the Physical Properties of Blast Waves* (Springer) 2016, pp. 53–86.
[2] Dewey J. M., *Proc. R. Soc. A: Math. Phys. Sci.*, **279** (1964) 366.
[3] Reed J. W., *J. Acoust. Soc. Am.*, **61** (1977) 39.
[4] Taylor G. I., *Proc. R. Soc. A: Math. Phys. Sci.*, **201** (1950) 175.
[5] Xu G., Conforti M., Kudlinski A., Mussot A. and Trillo S., *Phys. Rev. Lett.*, **118** (2017) 254101.
[6] Li Z., Zhang D., Yu B. and Guan L., *Eur. Phys. J. Appl. Phys.*, **28** (2004) 205.
[7] Hoefer M. A., Ablowitz M. J. and Engels P., *Phys. Rev. Lett.*, **100** (2008) 084504.
[8] Dewey J. M., *The Friedlander Equations* in *Blast Effects* (Springer) 2018, pp. 37–55.
[9] Friedlander F. G., *Proc. R. Soc. A: Math. Phys. Sci.*, **186** (1946) 322.
[10] Hoefer M. A., Ablowitz M. J., Coddington I., Cornell E. A., Engels P. and Schweikhard V., *Phys. Rev. A*, **74** (2006) 023623.
[11] Meppelink R., Koller S. B., Vogels J. M., van der Straten P., van Ooijen E. D., Heckenberg N. R., Rubinsztein-Dunlop H., Haine S. A. and Davis M. J., *Phys. Rev. A*, **80** (2009) 043606.
[12] Chang J. J., Engels P. and Hoefer M. A., *Phys. Rev. Lett.*, **101** (2008) 170404.
[13] Wan W., Jia S. and Fleischer J. W., *Nat. Phys.*, **3** (2007) 46.
[14] Conti C., Fratalocchi A., Peccianti M., Ruocco G. and Trillo S., *Phys. Rev. Lett.*, **102** (2009) 083902.
[15] Ghofraniha N., Gentilini S., Folli V., DelRe E. and Conti C., *Phys. Rev. Lett.*, **109** (2012) 243902.
[16] Carusotto I., *Proc. R. Soc. A: Math. Phys. Eng. Sci.*, **470** (2014) 20140320.
[17] Isoard M., Kamchatnov A. M. and Pavloff N., *Phys. Rev. A*, **99** (2019) 053819.
[18] Bienaimé T., Isoard M., Fontaine Q., Bramati A., Kamchatnov A., Glorieux Q. and Pavloff N., *Phys. Rev. Lett.*, **126** (2021) 183901.
[19] Ghofraniha N., Conti C., Ruocco G. and Trillo S., *Phys. Rev. Lett.*, **99** (2007) 043903.
[20] Wetzel B., Bongiovanni D., Kues M., Hu Y., Chen Z., Trillo S., Dudley J. M., Wabnitz S. and Morandotti R., *Phys. Rev. Lett.*, **117** (2016) 073902.
[21] Sadot O., Ram O., Nof E., Kochavi E. and Ben-Dor G., *Small-scale blast wave experiments by means of an exploding wire*, in *Blast Effects* (Springer) 2018.
[22] Pavloff N., *Optical hydrodynamics and nonlinear diffraction*, presented at *Waves Côte d'Azur* (2019).
[23] Fontaine Q., Bienaimé T., Pigeon S., Giacobino E., Bramati A. and Glorieux Q., *Phys. Rev. Lett.*, **121** (2018) 183604.
[24] Fontaine Q., Larré P.-É., Lerario G., Bienaimé T., Pigeon S., Faccio D., Carusotto I., Giacobino É., Bramati A. and Glorieux Q., *Phys. Rev. Res.*, **2** (2020) 043297.
[25] Piekarski C., Liu W., Steinhauer J., Giacobino E., Bramati A. and Glorieux Q., arXiv:2011.12935 (2020).
[26] Agha I. H., Giarmatzi C., Glorieux Q., Coudreau T., Grangier P. and Messin G., *New J. Phys.*, **13** (2011) 043030.
[27] Neuhaus L., Metzdorff R., Chua S., Jacqmin T., Briant T., Heidmann A., Cohadon P.-F. and Deléglise S., *Pyrpl - An Open-source Software Package for FPGA-controlled Quantum Optics Experiments* (Optical Society of America) 2017.
[28] Voronov B., Korobov A. and Rudenko O. V., *Sov. Phys. Usp.*, **35** (1992) 796.
[29] Rodrigues J. D., Mendonça J. T. and Terças H., *Phys. Rev. A*, **101** (2020) 043810.